

Spectral Photon-Counting Computed Tomography for Coronary Stent Imaging

Evaluation of the Potential Clinical Impact for the Delineation of In-Stent Restenosis

Grischa Bratke, MD,* Tilman Hieckethier, MD,* Daniel Bar-Ness, PhD,†‡ Alexander Christian Bunck, MD,* David Maintz, MD,* Gregor Pahn,§ Philippe Coulon, PhD,|| Salim Si-Mohamed, MD,†¶ Philippe Douek, MD, PhD,†¶ and Monica Sigovan, PhD†

Objectives: In-stent restenosis (ISR) is one of the main long-term complications after coronary stent placement, and the ability to evaluate ISR noninvasively using coronary computed tomography (CT) angiography remains challenging. For this application, spectral photon-counting CT (SPCCT) has the potential to increase image quality and reduce artifacts due to its advanced detector technology.

Our study aimed to verify the technical and clinical potential of a novel SPCCT prototype using an ISR phantom setup.

Materials and Methods: Soft plaque-like restenosis (45 HU; approximately 50% of the stent lumen) were inserted into 10 different coronary stents (3 mm diameter), which were placed in a vessel phantom and filled with a contrast agent (400 HU). A research prototype SPCCT and a clinical dual-layer CT (DLCT; IQon; Philips) with comparable acquisition and reconstruction parameters were used to scan the phantoms. Conventional polyenergetic (PolyE) and monoenergetic (MonoE) images with 4 different energy levels (40, 60, 90, 120 keV) were reconstructed. Qualitative (delineation of the stenosis and adjacent residual lumen using a 5-point Likert scale) and quantitative (image noise, visible lumen diameter, lumen diameter adjacent to the stenosis, contrast-to-noise ratio of the restenosis) parameters were evaluated for both systems.

Results: The qualitative results averaged over all reconstructions were significantly superior for SPCCT compared with DLCT (eg, subjective rating of the best reconstruction of each scanner: DLCT PolyE: 2.80 ± 0.42 vs SPCCT MonoE 40 keV: 4.25 ± 1.03). Stenosis could be clearly detected in 9 and suspected in 10 of the 10 stents with both SPCCT and DLCT. The residual lumen next to the stenosis was clearly delineable in 7 of 10 stents (0.64 ± 0.11 mm or 34.97% of the measured stent lumen) with SPCCT, while it was not possible to delineate the residual lumen for all stents using DLCT. The measured diameter of the lumen within the stent was significantly higher for SPCCT compared with DLCT in all reconstructions with the best results for the MonoE 40 keV images (SPCCT: 1.80 ± 0.17 mm; DLCT: 1.50 ± 0.31 mm). The image noise and the contrast-to-noise ratio were better for DLCT than for SPCCT (contrast-to-noise ratio: DLCT MonoE 40: 31.58 ± 12.54 ; SPCCT MonoE 40: 4.64 ± 1.30).

Conclusions: Spectral photon-counting CT allowed for the noninvasive evaluation of ISR with reliable results regarding the residual lumen for most tested

stents and the clear identification or suspicion of stenosis for all stents. In contrast, the residual lumen could not be detected for a single stent using DLCT.

Key Words: photon-counting, dual energy, computed tomography, CT, stent, cardiac, dual layer, coronary, restenosis, artery

(Invest Radiol 2019;00: 00–00)

Replacing invasive cardiac catheter examinations by noninvasive coronary computed tomography angiography (CCTA) scans is very desirable due to the risk for potential adverse events of cardiac catheterization (1.7% for a severe complication and 0.1% for mortality).¹ However, the application of CCTA is partially limited due to technical reasons, especially beam hardening and blooming.² Several recent technical improvements, including different reconstruction algorithms³ and spectral imaging,⁴ have led to increased accuracy of stenosis quantification mainly by artifact reduction. However, the exact evaluation of stent lumen and the delineation of possible in-stent restenosis (ISR) remains challenging with a significant number of unsatisfying ISR evaluation results. Eckert et al⁵ found 25% false-positive or inconclusive findings, and Li et al⁶ found a positive predictive value of 82.2% for all stents and only 68.2% for small caliber stents.

Novel spectral photon-counting CT (SPCCT) systems equipped with photon-counting detectors can overcome some of the technical shortcomings associated with CCTA due to 2 inherently different technological aspects. Photon-counting detectors have a continuous sensor layer which converts the incoming x-ray photon directly into electrical charges.⁷ The direct conversion of the photons makes the use of optical nontransparent separators unnecessary and results in an increased dose-efficiency and smaller pixel size of the detector. The incoming photons are also spectrally discriminated with pulse height analysis in multiple energy windows and therefore offer high-quality spectral capabilities.⁸ Recent studies have already shown improvements in image quality of in vitro stent imaging for PCD scanners with better in-stent lumen delineation and reduced blooming artifacts.^{9–11} However, from a clinical perspective, the question remains, whether these incremental advancements result in a real change of diagnostic capabilities, namely, the ability to delineate both the stenosis itself and the adjacent residual lumen. If so, this option for a noninvasive exact quantification or exclusion of in-stent stenosis could truly reduce the number of diagnostic catheterizations and therefore decrease unnecessary adverse events.

This in vitro study compared the visibility of artificial in-stent stenosis in different coronary stents using spectral dual-layer CT (DLCT) and SPCCT.

MATERIALS AND METHODS

Phantom

A straight plastic tube with a 3-mm diameter was used as a coronary artery phantom. The material had a wall thickness of 0.3 mm with an attenuation comparable to a vessel wall (35 Hounsfield Units [HU]).

Received for publication April 30, 2019; and accepted for publication, after revision, July 14, 2019.

From the *Department of Radiology, University of Cologne, Cologne, Germany; †Creatis Laboratory, CNRS UMR 5220, INSERM U12063, University Claude Bernard Lyon 1; ‡CERMEP-Imagerie du Vivant, Lyon, France; §Philips GmbH Healthcare Division, Hamburg, Germany; ||Philips, CT Clinical Science, Suresnes; and ¶Radiology Department, Hospices Civils de Lyon, Lyon, France.

Grischa Bratke and Tilman Hieckethier contributed equally to this work.

Conflicts of interest and sources of funding: G. Pahn, P. Coulon, and Y. Yagil are currently working for Philips. For the remaining authors, none were declared.

Supplemental digital contents are available for this article. Direct URL citations appear in the printed text and are provided in the HTML and PDF versions of this article on the journal's Web site (www.investigativeradiology.com).

Correspondence to: Grischa Bratke, MD, Department of Radiology, University of Cologne, Kerpenerstr. 62, 50937 Cologne, Germany. E-mail: grischa.bratke@uk-koeln.de.

Copyright © 2019 Wolters Kluwer Health, Inc. All rights reserved.

ISSN: 0020-9996/19/0000-0000

DOI: 10.1097/RLI.0000000000000610

TABLE 1. Parameters of the Used Stents

Stent	Material	Strut Thickness, mm	Length, mm
Chrono (Sorin Biomedical)	Cobalt-chrome (CoCr)	0.08	20
Endeavor (Medtronic)	CoCr	0.091	30
Prokinetic (Biotronik)	CoCr	0.06	15
Radius (Boston Scientific)	Nitinol	0.085	20
Omega (Boston Scientific)	PICr	0.081	16
Promus Element Plus (Boston Scientific)	PICr	0.081	19
Coroflex Please (Braun)	Stainless steel 316L	0.12	19
Tenax XR (Biotronik)	Stainless steel 316L	0.08	15
Tantal Coronary (Abbott/Guidant)	Tantalum	0.58	19
Wiktor (Medtronic)	Tantalum	0.064	30

CoCr indicates cobalt-chrome; PICr, platinum chromium.

Ten different stents (Table 1) made of 5 different materials were used to account for the broad variety of commercially available stents and to verify the clinical reliability. The stents were placed in the middle of the plastic tube with an average length of 20.3 mm (± 5.18 mm) and a strut thickness of 0.13 mm (± 0.15 mm). The artificial hypodense stenoses were made of a wax-based material mixed with ethiodized oil (Lipiodol Ultra-Fluid; Guerbet GmbH, Sulzbach, Germany) titrated to measure 45 HU at 120 kVp. This was chosen because in stented lesions the late lumen loss and restenosis are mainly the result of neointimal tissue proliferation with similar densities.¹² The grain-shaped restenoses were positioned angiographically guided inside the stented tube lumen. To calibrate each stenosis to 50% of the total diameter, the stenosis was passed with a 1.5-mm balloon catheter (Armada 14; Abbott GmbH, Wiesbaden, Germany) using a microwire (V-14 Control Wire; Boston Scientific GmbH, Ratingen, Germany). After verification of the correct position, the balloon was inflated to its nominal pressure. The tube was filled with the iodine-based contrast agent iohexal (300 mg/mL; Accupaque 300; GE Healthcare GmbH, Solingen, Germany), which was diluted with saline solution to a density of 400 HU at 120 kV/100 mAs using DLCT. The tube was placed in a plastic container (36 × 24 cm), which was fluid-filled (sodium chloride). The phantoms were placed in the isocenter of each scanner parallel to the z-axis.

CT Acquisition and Reconstruction Parameters

The acquisition parameters for both CT scanners were chosen to keep the differences between the systems as minimal as possible (Table 2).

The SPCCT prototype used a cadmium zinc telluride-based PCD. The highest possible resolution was chosen with a collimation of 9×0.25 mm and a slice thickness of 0.25 mm. Tube current was set to 100 mAs with 120 kVp and a rotation time of 1 second. The images were reconstructed with a sharp filter, an image matrix of 512×512 pixels, and a field of view of 102 mm. Conventional polyenergetic (PolyE) and 4 different monoenergetic (MonoE) images (40, 60, 90, 120 keV) were reconstructed. For the used SPCCT prototype, only filtered back projection was available as reconstruction method without any iterative reconstruction algorithms. Further technical details concerning this prototype system are provided in previous publications.^{13,14}

For comparison, dual-energy CT data were acquired on a 128-row DLCT scanner (IQon; Philips Healthcare, Best, the Netherlands). Acquisition parameters for the DLCT were a collimation of 64×0.625 mm with the thinnest possible slice thickness of 0.67 mm and a rotation time of 0.27 second. This also represents our current clinical standard for CCTA. In line with SPCCT parameters, the tube current was set to 100 mAs with 120 kV without automatic dose modulation. The images

TABLE 2. CT Acquisition and Reconstruction Parameters of Both Systems

	SPCCT	DLCT
Scan type	Axial	Axial
Collimation	9×0.25 mm	64×0.625 mm
Focal spot resolution	High	Standard
Slice thickness	0.25 mm	0.67 mm
Rotation time	1 s	0.27 s
Voltage	120 kV	120 kV
Current	100 mA/100 mAs	368 mA/100 mAs
Dose modulation	None	None
Image matrix	512×512	512×512
Field of view	102 mm	102 mm
Reconstruction filter	Sharp	CD (cardiac detailed stent)
Iterative reconstruction	No	As low as possible (iDose/Spectral Level 0)

Since SPCCT was a research prototype, not every option of commercial scanners was available, and the DLCT parameters had to be adapted to it.

CT indicates computed tomography; SPCCT, spectral photon-counting CT; DLCT, dual-layer CT.

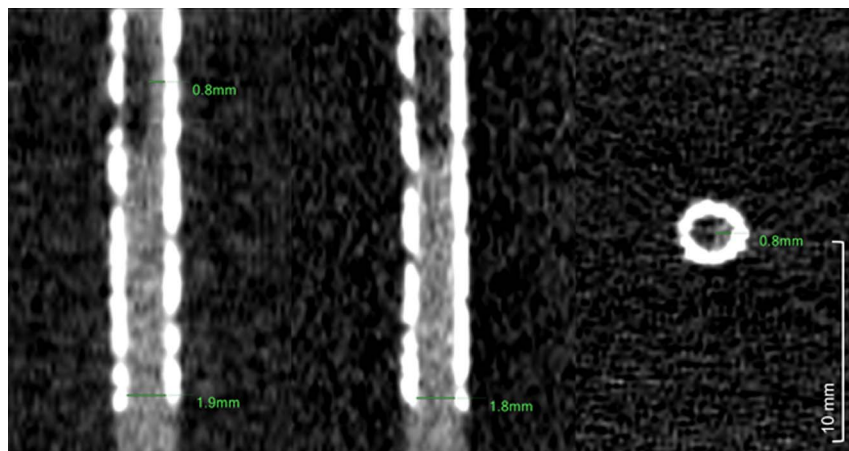


FIGURE 1. Coronal, sagittal, and axial reconstruction of the Coroflex stent in spectral photon-counting computed tomography PolyE images of the SPCCT with measurements of the in-stent lumen and the residual lumen. The manual positioning of the artificial stenosis led to eccentric positions and therefore the residual lumen was averaged from the 2 largest measurements.

were calculated with a dedicated cardiac stent reconstructions filter and the iterative reconstruction components set to level 0. This was the most comparable setting that could be achieved for DLCT as plain filtered back projection without any iterative component was not available on this commercial system.

Data Analysis

Multiplanar reformats in coronary, axial, and sagittal orientation were reconstructed on the same offline workstation for all images (IntelliSpace Portal; Philips Healthcare, Best, the Netherlands) with a thickness equal to that of the underlying slice stack. Two raters (R1 and R2, with 6 and 5 years of experience in cardiovascular imaging, respectively) performed an independent quantitative and qualitative analysis of all available images.

Quantitative Analysis

In-stent diameter and visible residual lumen next to the stenosis were measured by both raters with an electronic caliper tool (Fig. 1).

Reader 2 additionally measured the attenuation in Hounsfield Units (HU) with standardized regions of interest (ROIs) in the tube lumen outside the stent (ROI 1), in the stent (ROI 2), and in the stenosis (ROI 3), as well as the standard deviation of the attenuation outside the tube in the surrounding container (ROI 4; Fig. 2). The difference in the stenosis density was calculated as that between the density of the stenosis (ROI 3) and the density inside the stent beside the stenosis (ROI 2). The in-stent attenuation difference between the lumen outside (ROI 1) and within the stent (ROI 2) was calculated by subtracting the corresponding ROIs accordingly. To avoid potential interreader differences due to different window settings, predefined parameters for the window center and width for each reconstruction were used. The window level was equal to the density of the ROI measurement in the tube volume outside the stent (ROI 1) for each reconstruction. According to previous findings,¹⁵ the window width was then set to a multiplication of the level value, which was set to a factor of 2.5 based on a consensus reading. The diameter was determined next to the end of the stent in the coronal and sagittal reformation (average of both measurements). At the

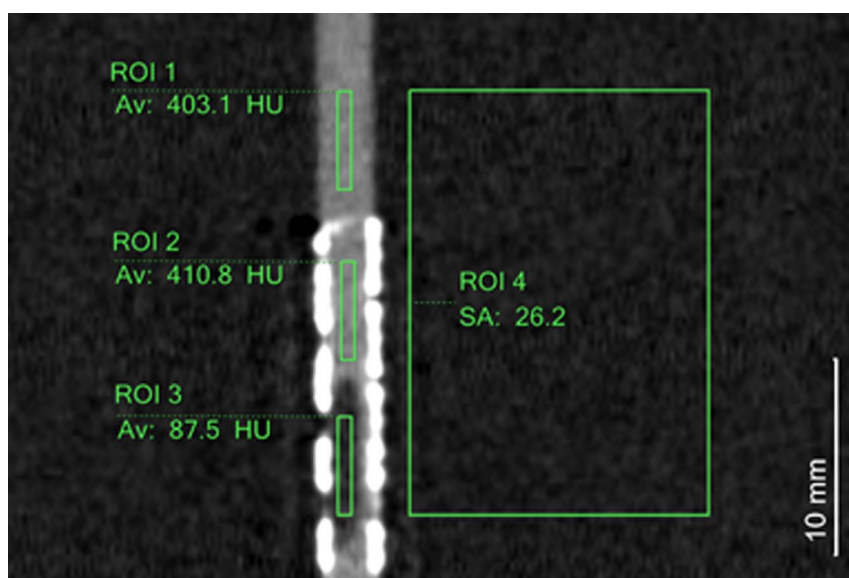


FIGURE 2. Measurement of the different regions of interest (ROI) in the PolyE image for the Chrono stent with spectral photon-counting computed tomography. The first ROI was placed in the lumen of the artificial vessel. ROI 2 represents the attenuation of the contrast agent within the stent and ROI 3 within the stenosis. ROI 4 is outside of the artificial vessel to measure the overall image noise.

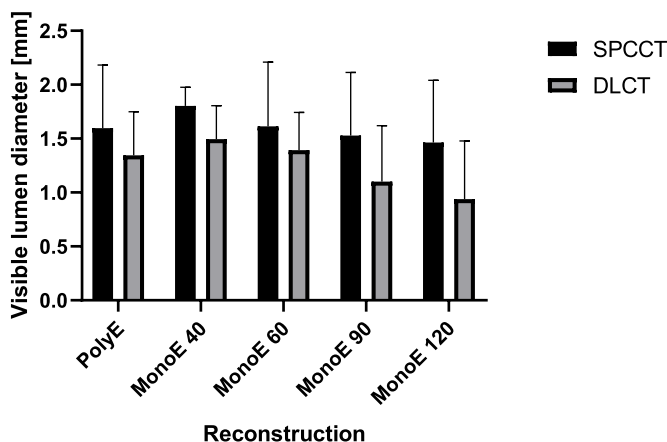


FIGURE 3. Diameter of the in-stent lumen. A clear trend toward better quantitative delineation of the stent diameter for spectral photon-counting computed tomography compared with the dual-layer computed tomography, and for PolyE and low MonoE keV compared with high MonoE keV was observed without reaching statistical significance.

middle of the stenosis, the size of the residual lumen was measured on the coronal, sagittal, and axial reformations. Due to the eccentric shape and position of the artificial stenosis, the average of the 2 largest diameters was used. The standard deviation of the density in the surrounding liquid (ROI 4) served as a parameter for the image noise. The contrast-to-noise ratio (CNR) of the stenosis was calculated as the difference in the stenosis density divided by the image noise.

Qualitative Analysis

Both readers evaluated the subjective visibility of the stenosis and the remaining lumen on the coronal, axial, and longitudinal multiplanar reformat images using a 5-point Likert scale (1, image quality impedes lumen assessment and stenosis not visible; 2, lumen appears stenosed with unclear extent; 3, stenosis and extent clear, but residual lumen undistinguishable; 4, stenosis clear and residual lumen distinguishable; and 5, stenosis and residual lumen clear).

Statistical Analysis

Statistical analyses were performed using GraphPad Prism Version 8.0.2 (GraphPad Software Inc, San Diego, CA). All data are reported as the mean ± standard deviation (SD). For the ordinal data of the subjective reading, the Friedman test was used, followed by Dunn's multiple comparisons post hoc test. The different quantitative parameters with continuous data were tested for significance with a one-way analysis of

TABLE 3. Visible Diameter of the In-Stent and Residual Lumen Averaged for Both Raters

Reconstruction	Visible Lumen Diameter, mm		Residual Lumen, mm	
	SPCCT	DLCT	SPCCT	DLCT
PolyE	1.60 ± 0.59	1.35 ± 0.40	0.45 ± 0.32	0
MonoE 40	1.80 ± 0.17	1.50 ± 0.31	0.44 ± 0.31	0
MonoE 60	1.61 ± 0.60	1.39 ± 0.35	0.43 ± 0.31	0
MonoE 90	1.53 ± 0.59	1.10 ± 0.52	0.36 ± 0.27	0
MonoE 120	1.46 ± 0.58	0.94 ± 0.54	0.14 ± 0.21	0

SPCCT indicates spectral photon-counting computed tomography; DLCT, dual-layer computed tomography.

variance, Tukey test for post hoc analysis for the different reconstructions for a single scanner, and the Bonferroni test for the comparison of the same reconstruction between different scanners. A P value of less than 0.05 was considered statistically significant. The interrater agreement for the in-stent and residual lumen measurements was tested with the Pearson correlation coefficient and the subjective scoring with Cohen kappa. According to Landis and Koch,¹⁶ values of 0.61 to 0.80 were interpreted as substantial, and 0.81 to 1.00, as almost perfect agreement.

RESULTS

Lumen Assessment

The interrater agreement between both the raters was almost perfect for measurements of the in-stent lumen (r = 0.97) and residual lumen next to the stenosis (r = 0.99). The average measured lumen of the stents for all reconstructions was significantly higher for SPCCT than for DLCT (P = 0.001). The highest measured lumen for SPCCT was 1.83 ± 0.17 mm in MonoE 40 keV images and 1.50 ± 0.31 mm for the DLCT with MonoE 40 keV (Fig. 3, Table 3). Despite the clear trend for a higher measured lumen in the low energetic MonoE images, there was no statistically significant difference between the different reconstructions within each scanner.

The residual lumen was not visible in any reconstruction of DLCT images, and therefore, the measured residual lumen was 0 mm in all DLCT reconstructions and stents. For SPCCT, the best delineation of the residual lumen was achieved with the PolyE reconstructions with an average measured diameter of 0.45 ± 0.32 mm. Among different SPCCT reconstructions, the results were significantly better for the PolyE (P = 0.011), MonoE 40 keV (P = 0.015), and MonoE 60 images (P = 0.018) than for the high energetic MonoE 120 keV images (Fig. 4, Table 3). In addition, the residual lumen was rated as distinguishable in at least one reconstruction in 7 of the 10 stents. The average residual lumen of these 7 stents was 0.64 ± 0.11 mm in the PolyE reconstruction, which is equal to 34.97% of the measured total lumen or 43% of the real residual lumen.

ROI-Based Density Analysis

For the Wiktor stent, the artifacts due to beam hardening affected the image quality so much that the exact extent of stenosis could not be detected on any reconstruction for both scanners, making a reliable

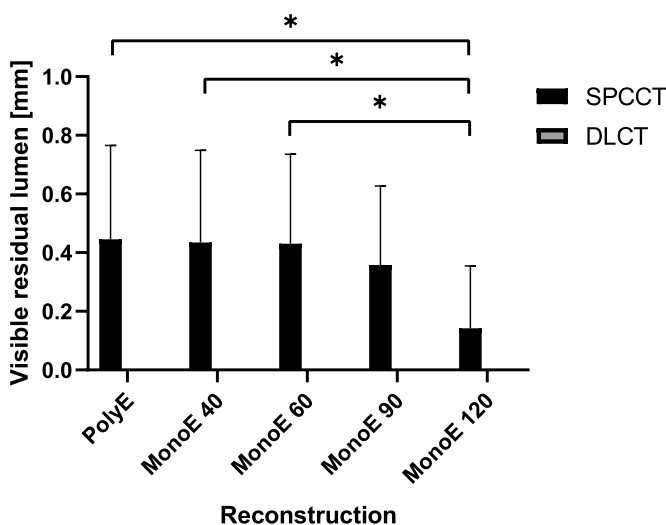


FIGURE 4. Residual lumen of all 10 stents. No residual lumen could be depicted for dual-layer computed tomography. The values for PolyE and lower keV images are comparable and significantly higher than for 120 keV reconstructions (all P < 0.05).

TABLE 4. Quantitative Image Quality Parameters

Reconstruction	Image Noise, HU		Stenosis Density Difference, HU	
	SPCCT	DLCT	SPCCT	DLCT
PolyE	41.36 ± 7.18	37.29 ± 7.04	345.13 ± 17.75	356.68 ± 190.08
MonoE 40	158.47 ± 24.29	35.79 ± 9.31	667.16 ± 49.52	1037.88 ± 257.26
MonoE 60	44.26 ± 8.70	28.96 ± 5.15	355.17 ± 26.41	489.34 ± 83.28
MonoE 90	79.88 ± 12.78	28.27 ± 4.68	221.66 ± 39.74	289.01 ± 159.86
MonoE 120	98.79 ± 15.48	28.45 ± 4.73	173.42 ± 41.72	226.37 ± 167.77

SPCCT indicates spectral photon-counting computed tomography; DLCT, dual-layer computed tomography.

measurement of the attenuation in the stent and stenosis impossible. To avoid the potential influence of a wrongly placed measurement, the stent was excluded from the following ROI-based analysis.

In line with previous dual-energy studies, the attenuation within the tube lumen differed significantly depending on the chosen reconstruction with the highest attenuation for the low keV MonoE images and the lowest for the high keV MonoE images (Supplementary Table 1 for detailed results, Supplemental Digital Content, <http://links.lww.com/RLI/A472>). The attenuation was higher within the stent (ROI 2) compared with the ROI outside the stent (ROI 1) for both scanners due to beam hardening caused by the surrounding stent material. Averaged overall reconstructions, the SPCCT showed a significant smaller in-stent attenuation difference ($P = 0.025$); however, none of the individual reconstructions were superior compared with other reconstructions of the same scanner or the same reconstruction on the other scanner. For SPCCT, the MonoE 40 keV (67.31 ± 45.48 HU) showed the largest difference, with the smallest observed in the MonoE 120 keV images (48.88 ± 82.88 HU). For DLCT, however, the MonoE 40 keV images had a smaller difference (94.78 ± 51.48) than the MonoE 120 keV images (178.49 ± 306.27), and the PolyE images provided the lowest in-stent attenuation difference (69.20 ± 39.45 HU; Supplementary Table 1, Supplemental Digital Content, <http://links.lww.com/RLI/A472>). The high variability observed with DLCT was caused mainly by the Tantal stent and its artifacts within the stent lumen (ROI 2).

Overall, stenosis density differences were significantly higher for DLCT than SPCCT ($P < 0.001$). When comparing the individual reconstructions of both systems, the MonoE 40 keV ($P < 0.001$) and MonoE 60 keV images ($P = 0.005$) of the DLCT were superior to the corresponding SPCCT images. For both scanners, the MonoE 40 keV images were superior over all other reconstructions (all $P \leq 0.001$; Table 4).

The noise measured in the fluid next to the stents was significantly higher for SPCCT than DLCT (all $P < 0.001$; eg, for MonoE 40 keV: SPCCT 158.47 ± 24.29 HU, DLCT 25.79 ± 9.31 HU; Table 4). There were no significant differences in the image noise for the different

DLCT reconstructions. For SPCCT, however, image noise was significantly higher (all $P < 0.05$) in low (MonoE 40) and high (MonoE 90 and MonoE 120) energetic MonoE reconstructions compared with the PolyE and 60 keV MonoE images (which had comparable noise levels).

Due to the higher stenosis density differences and lower image noise, CNR was significantly higher in DLCT images than in the corresponding SPCCT images ($P < 0.001$; Table 5). MonoE 40 keV DLCT images showed the highest overall CNR values (31.18 ± 13.57), which were significantly higher than in any other reconstruction (all $P < 0.05$). For SPCCT, the PolyE images offered the best CNR with a mean value of 8.67 ± 2.25 .

Qualitative Analysis

The interrater agreement for the subjective scoring was almost perfect with a kappa of 0.84. Throughout every reconstruction, the qualitative analysis showed superior scores for SPCCT (Figs. 5, 6) with an overall significantly better subjective rating ($P < 0.001$; Table 5). There was a visible trend to higher scores for SPCCT images of the corresponding reconstructions of both scanners, which did not reach statistical significance, for example, SPCCT MonoE 60 keV with 3.95 ± 1.46 and DLCT MonoE 60 keV with 2.5 ± 0.71 ($P = 0.60$). MonoE 40 keV resulted in the best rating for SPCCT with 4.25 ± 1.03 compared with PolyE as the best reconstruction for DLCT at 2.80 ± 0.42 ($P = 0.90$).

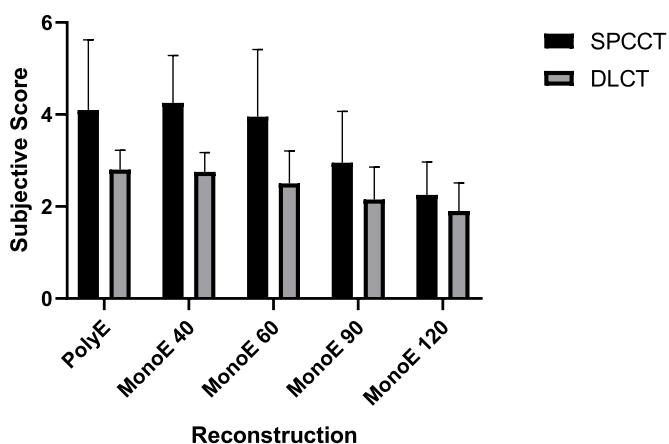


FIGURE 5. Subjective scoring averaged for both raters. The spectral photon-counting computed tomography (SPCCT) offered a significantly better image quality ($P < 0.0001$) if averaged for all reconstructions with the best scores for MonoE 40 images. The ratings were higher for every SPCCT image compared with the corresponding dual-layer computed-tomography (DLCT) images. The PolyE, MonoE 40 keV, and MonoE 60 keV reconstructions of the SPCCT images show significantly better subjective ratings than the MonoE 120 keV SPCCT as well as the MonoE 90 keV and 120 keV DLCT images (all $P < 0.05$).

TABLE 5. CNR Values and Subjective Scores of Both Systems

Reconstruction	CNR		Subjective Score	
	SPCCT	DLCT	SPCCT	DLCT
PolyE	9.00 ± 3.22	10.79 ± 4.86	4.10 ± 1.52	2.80 ± 0.42
MonoE 40	4.46 ± 1.30	31.58 ± 12.54	4.25 ± 1.03	2.75 ± 0.23
MonoE 60	8.42 ± 2.17	17.08 ± 4.03	3.95 ± 1.46	2.50 ± 0.71
MonoE 90	2.95 ± 1.05	9.36 ± 2.63	2.95 ± 1.12	2.15 ± 0.71
MonoE 120	1.88 ± 0.27	6.62 ± 2.42	2.25 ± 0.72	1.90 ± 0.62

CNR indicates contrast-to-noise ratio; SPCCT, spectral photon-counting computed tomography; DLCT, dual-layer computed tomography.

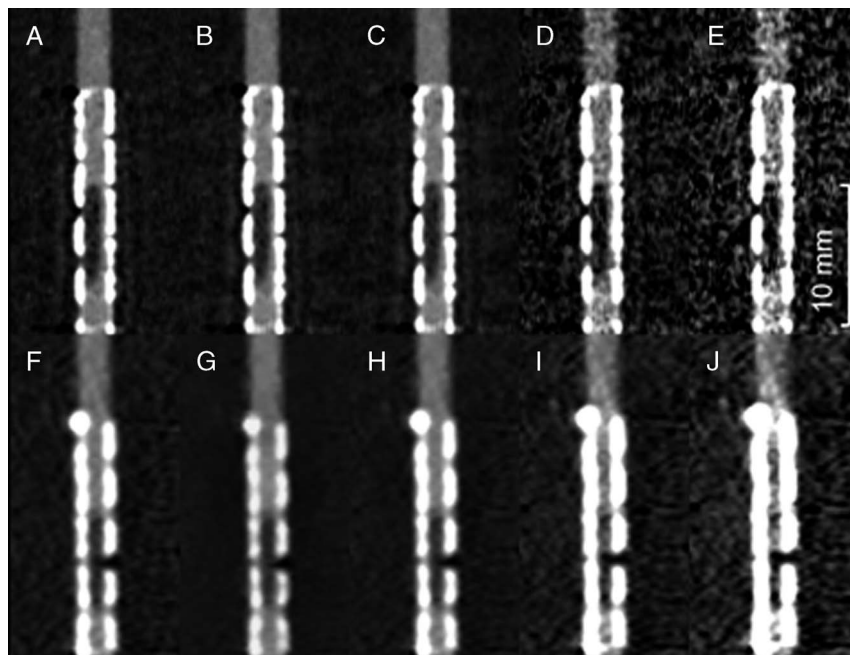


FIGURE 6. Comparison of the different reconstructions for the spectral photon-counting computed tomography (A–E) and dual-layer computed tomography (F–J) with the Chrono stent and the individually adapted window settings. For both scanners, delineation of the stenosis was better for PolyE (A and F) and MonoE 40 keV (B and G) images compared with higher keV images (MonoE 60, C and H; MonoE 90, D and I) and especially MonoE 120 keV (E and J). The different window settings were optimized to delineate the stenosis but also influenced the artifact blooming and overall image noise.

For both scanners, the stenosis was clearly detectable in 9 of 10 stents (rating ≥ 3) and suspected in all stents (rating ≥ 2).

DISCUSSION

The use of SPCCT for stent imaging offered a superior subjective image quality, which can result in completely new diagnostic capabilities and may potentially enable additional applications for CCTA. A clear evaluation of the in-stent stenosis and adjacent residual lumen was possible and allowed for highly reliable noninvasive assessments of the actual extent of stenosis in nearly all tested stents. The PolyE images showed a good overall delineation for the different materials, and the spectral MonoE images allowed for an additional reduction of stent-related artifacts and better visualization of the stent lumen. Potential stenoses could be detected for all the tested stents using the low-energetic MonoE reconstructions, and a clear visualization of ISR was possible in 90% of cases, whereas the PolyE images were occasionally impaired by artifacts of the stent material (especially by Tantalum), and stenosis was suspected in only 80% of cases.

The parameters for DLCT were selected to align as closely as possible to SPCCT. Therefore, further improvements in DLCT image quality by utilizing optimized acquisition and reconstruction parameters might be possible; however, the detector resolution would still be the limiting factor. In addition, our results with a clear detection of the stenosis for 80% of the tested stents and a suspicion in 90% of the cases are in line with previous studies testing the diagnostic quality of different CT systems^{5,6,17}; thus, the influence of our used acquisition and reconstruction parameters on the overall results is likely limited. For both systems, the thinnest possible slice was chosen, which resulted in the SPCCT thickness being less than half the thickness of DLCT. The thinner slice thickness caused increased noise for the SPCCT images. This is supported by the results from another *in vitro* stent study by Almutairi et al,¹⁸ which found that image noise increased by a factor of 2.7 when

the slice thickness was reduced from 1.5 to 0.67 mm. On the other hand, the thinner slice thickness might assist with the discrimination of smaller structures and reduces potential partial volume effects that could occur in an *in vivo* setting and could therefore increase the effective noise level. Specifically, an eccentric position of the stent with respect to the z-axis increases partial volume effects of the stent material within the lumen, which can only be reduced by a thinner slice thickness. The used prototype SPCCT is only capable of using filtered back projection. Further developments in SPCCT image processing are expected to reduce image noise for this system and would therefore potentially allow for the achievement of better CNR values than DLCT. von Spiczak et al¹⁰ have already shown that the application of an iterative reconstruction algorithm for a SPCCT prototype of a different vendor could decrease the image noise by 41 to 59%. A comparable reduction would reduce the noise level of SPCCT even below DLCT values for some reconstructions. In line with previous results of Hickethier et al,¹⁹ we found a significant reduction of blooming artifacts with the application of higher-energy levels. However, adjusting window settings to the individual attenuation of each reconstruction did not lead to an increase in the overall measured lumen in our study; however, there was even a trend toward higher values for low keV images observed. For SPCCT, the measured lumen was significantly closer to the real stent diameter of 3 mm compared with DLCT. The identification of stenoses was enhanced by using lower-energy levels due to the increased attenuation difference between the hypodense stenotic material and the contrast agent in the adjacent vessel lumen.

Although drug-eluting stents significantly reduce the number of in-stent stenoses,²⁰ these are still highly relevant complications,²¹ which adversely affect clinical outcomes.^{22,23} Bossi et al found the pattern of the in-stent stenosis as well as the time to ISR less than 90 days to be independent predictors for subsequent revascularization.²⁴ Therefore, the possibility for noninvasive assessment and exact measurement of the stenosis would be highly desirable, especially because ISR can be

diagnosed without specific symptoms.¹⁶ Future screening with SPCCT might be an option to identify ISR and select patients in need of angioplasty. This is especially valuable since the application of noninvasive diagnostic tests not only reduces the amount of potential side effects, but also reduces the costs per patient. Min et al²⁵ found that the use of CCTA (assuming 90% sensitivity and 96% specificity) for patients with suspected ISR can reduce the cost per stented patient to less than 30% of the invasive strategy with direct referral to invasive coronary angiography for all patients (US \$490 vs US \$1656).

The main limitation of this study was the in vitro design as a proof-of-concept. Possible motion artifacts in patients could result in inferior image quality. In addition, all stents had a diameter of 3 mm, which was considered as the lower limit for large caliber stents by Li et al⁶ with better accuracy. Additional studies need to test whether the lumen will be still visible for stents with smaller diameters. The grade of the stenosis was overrated on average with 65% instead of the true 50% for the stents with a subjective scoring of 4 or better. Calcification of the imitated vessel was completely absent, which might influence the overall image quality or stenosis delineation; however, spectral reconstructions already showed to have the potential of reducing the related artifacts as well (similar to the stent artifacts).⁴ In addition, in our study, a clinically desirable concentration of the contrast agent within the vessel phantom was chosen to evaluate the performance potential. Results with suboptimal contrast conditions might be different and should be evaluated in further studies.

For noninvasive detection of ISR, we were able to demonstrate for the first time that the technical improvements of SPCCT yield clinically relevant additional information. The combination of higher resolution and spectral information enabled the detection or suspicion of an ISR in all tested stents. Therefore, SPCCT systems have the potential to reduce the need for invasive coronary angiographies with primary diagnostic purposes.

ACKNOWLEDGMENTS

The author would like to thank Yoad Yagil for constructive criticism of the manuscript.

REFERENCES

1. Noto TJ, Johnson LW, Krone R, et al. Cardiac catheterization 1990: a report of the registry of the society for cardiac angiography and interventions (SCA&I). *Cather Cardio Diag.* 1991;24:75–83.
2. Maintz D, Juergens KU, Wichter T, et al. Imaging of coronary artery stents using multislice computed tomography: in vitro evaluation. *Eur Radiol.* 2003;13:830–835.
3. Puchner SB, Ferencik M, Maehara A, et al. Iterative Image reconstruction improves the accuracy of automated plaque burden assessment in coronary CT angiography: a comparison with intravascular ultrasound. *Am J Roentgeno.* 2017;208:777–784.
4. Symons R, Choi Y, Cork TE, et al. Optimized energy of spectral coronary CT angiography for coronary plaque detection and quantification. *J Cardiovasc Comput Tomogr.* 2018;12:108–114.
5. Eckert J, Renczes-Janetzko P, Schmidt M, et al. Coronary CT angiography (CCTA) using third-generation dual-source CT for ruling out in-stent restenosis. *Clin Res Cardiol.* 2019;108:402–410. Available at: <https://doi.org/10.1007/s00392-018-1369-1>. Accessed January 27, 2019.
6. Li Y, Yu M, Li W, et al. Third generation dual-source CT enables accurate diagnosis of coronary restenosis in all size stents with low radiation dose and preserved image quality. *Eur Radiol.* 2018;28:2647–2654.
7. Taguchi K. Energy-sensitive photon counting detector-based X-ray computed tomography. *Radiol Phys Technol.* 2017;10:8–22.
8. Taguchi K, Iwanczyk JS. Vision 20/20: single photon counting x-ray detectors in medical imaging. *Med Phys.* 2013;40:100901.
9. Mannil M, Hickethier T, von Spiczak J, et al. Photon-counting CT: high-resolution imaging of coronary stents. *Invest Radiol.* 2018;53:143–149.
10. von Spiczak J, Mannil M, Peters B, et al. Photon counting computed tomography with dedicated sharp convolution kernels: tapping the potential of a new technology for stent imaging. *Invest Radiol.* 2018;53:486–494.
11. Symons R, De Bruecker Y, Roosen J, et al. Quarter-millimeter spectral coronary stent imaging with photon-counting CT: initial experience. *J Cardiovasc Comput.* 2018;12:509–515.
12. Hoffmann R, Mintz GS, Dussallant GR, et al. Patterns and mechanisms of in-stent restenosis. *Circulation.* 1996;94:1247–1254.
13. Kopp FK, Daerr H, Si-Mohamed S, et al. Evaluation of a preclinical photon-counting CT prototype for pulmonary imaging. *Sci Rep.* 2018;8:17386. Available at: <https://www.ncbi.nlm.nih.gov/pmc/articles/PMC6255779/>. Accessed April 29, 2019.
14. Si-Mohamed S, Thivolet A, Bonnot PE, et al. Improved peritoneal cavity and abdominal organ imaging using a biphasic contrast agent protocol and spectral photon counting computed tomography K-Edge Imaging. *Invest Radiol.* 2018;53:629–639.
15. Doerner J, Luettgens JA, Iuga AI, et al. Poly-energetic and virtual mono-energetic images from a novel dual-layer spectral detector CT: optimization of window settings is crucial to improve subjective image quality in abdominal CT angiographies. *Abdom Radiol.* 2018;43:742–750.
16. Landis JR, Koch GG. The measurement of observer agreement for categorical data. *Biometrics.* 1977;33:159–174.
17. Yang J, Yang X, De Cecco CN, et al. Iterative reconstruction improves detection of in-stent restenosis by high-pitch dual-source coronary CT angiography. *Sci Rep.* 2017;7:6956.
18. Almutairi AM, Sun Z, Ng C, et al. Optimal scanning protocols of 64-slice CT angiography in coronary artery stents: an in vitro phantom study. *Eur Radiol.* 2010;74:156–160.
19. Hickethier T, Baeßler B, Kroeger JR, et al. Monoenergetic reconstructions for imaging of coronary artery stents using spectral detector CT: In-vitro experience and comparison to conventional images. *J Cardiovasc Comput.* 2017;11:33–39.
20. Stettler C, Wandel S, Allemann S, et al. Outcomes associated with drug-eluting and bare-metal stents: a collaborative network meta-analysis. *Lancet.* 2007;370:937–948.
21. Smits PC, Vlachojannis GJ, McFadden EP, et al. Final 5-year follow-up of a randomized controlled trial of everolimus-and paclitaxel-eluting stents for coronary revascularization in daily practice: the COMPARE trial (A Trial of Everolimus-Eluting Stents and Paclitaxel Stents for Coronary Revascularization in Daily Practice). *J Am Coll Cardiol Intv.* 2015;8:1157–1165.
22. Bossi I, Klersy C, Black AJ, et al. In-stent restenosis: long-term outcome and predictors of subsequent target lesion revascularization after repeat balloon angioplasty. *J Am Coll Cardiol.* 2000;35:1569–1576.
23. Chen MS, John JM, Chew DP, et al. Bare metal stent restenosis is not a benign clinical entity. *Am Heart J.* 2006;151:1260–1264.
24. Alraies MC, Darmoch F, Tummala R, et al. Diagnosis and management challenges of in-stent restenosis in coronary arteries. *World J Cardiol.* 2017;9:640–651.
25. Min JK, Hasegawa JT, Machacz SF, et al. Costs and clinical outcomes for non-invasive versus invasive diagnostic approaches to patients with suspected in-stent restenosis. *Int J Cardiovasc Imaging.* 2016;32:309–315.